Research Article | Vol. 32, No. 13 / 17 Jun 2024 / Optics Express 22169
Optics EXPRESS

Modeling full PCSELs and VCSELs using modified rigorous coupled-wave analysis

JINGXIAO XU,[1,*] DOUGLAS MCCULLOCH,[2] AND MARTIN D. B. CHARLTON[1]

[1] School of Electronics and Computer Science, University of Southampton, SO17 1BJ Southampton, UK
[2] Zepler Institute, University of Southampton, SO17 1BJ Southampton, UK
[*] jx4n15@soton.ac.uk

Abstract: An integrated rigorous coupled-wave analysis (RCWA) algorithm is presented in this paper, which can simulate full vertical-cavity surface-emitting laser (VCSEL) and photonic crystal surface-emitting laser (PCSEL) structures. A classic RCWA can only analyze a structure when the light source is incident from the top, bottom, or both sides of the device. However, for VCSEL applications, the light source is generated in the middle and propagates in both directions. A bidirectional scattering matrix method and doubling algorithm are implemented in RCWA. The resonant wavelength and Q factor of a VCSEL can then be found in the output spectrum. The accuracy and execution speed are compared with those of the Lumerical finite-difference time-domain (FDTD) method for several VCSEL and PCSEL designs. The results show that the maximum discrepancy between RCWA and FDTD is less than 3 nm, and the difference in the far-field divergence angle is less than 0.5°. The speed of RCWA also outperforms FDTD simulation significantly.

1. Introduction

Vertical-cavity surface-emitting lasers (VCSELs) and photonic crystal surface-emitting lasers (PCSEL) are promising types of lasers that emit light perpendicular to the top surface. Compared with conventional edge-emitting lasers, VCSELs have numerous advantages, such as a low threshold current, low power dissipation, and on-wafer testing. Consequently, VCSELs have been extensively researched and employed in high-speed LANs [1], sensing [2], and optical communications [3]. In particular, VCSELs and PCSELs are gaining popularity in Light Detection and Ranging (LiDAR) applications owing to their high accuracy and energy efficiency [4,5]. One of the critical parameters in the design of VCSELs is the resonant wavelength, which can be calculated using various simulation methods. The resonant wavelength determines the optimal operating wavelength of a VCSEL, which can be found at the peaks in its output power spectrum [6,7]. Another critical parameter was the divergence angle of the laser beam. A narrow beam means that the laser maintains a high power over a longer distance. High-quality narrow-beam VCSELs and PCSELs are of interest to many researchers [8,9].

The Transfer Matrix Method (TMM) is a widely used numerical simulation method for one-dimensional Distributed Bragg Reflectors (DBRs). TMM only uses a 2*2-sized matrix, which is more effective than other computational methods, such as the finite-difference time-domain (FDTD), in simulating uniform layer structures [10]. However, if the VCSEL has nonuniform (grating or photonic crystal) layers, more complex numerical methods are required. The FDTD method has been used to determine the resonant wavelength and projection pattern of a VCSEL design [11,12]. Rigorous coupled-wave analysis (RCWA), also known as the Fourier model method (FMM), is a powerful method for simulating periodic structures [13–16]. Unfortunately, the conventional RCWA method is unable to solve full PCSEL or VCSEL structures where light

#522484 https://doi.org/10.1364/OE.522484
Journal © 2024 Received 27 Feb 2024; revised 23 May 2024; accepted 23 May 2024; published 3 Jun 2024

Optics EXPRESS

sources are positioned inside the device. Conventional multilayer linking methods in RCWA, such as the S-matrix [17], R-matrix [18], and Enhanced Transmittance Matrix [19], may function only with light sources incident from above or below the device. More methods have been developed to simulate PCSELs, such as coupled wave theory (CWT) [20,21] and a modified RCWA using first principles [22]. However, CWT utilizes several approximations during the computation, and the second method cannot provide field information.

This paper presents a new RCWA algorithm that can compute the diffraction efficiency and electromagnetic fields of a complete periodic VCSEL or PCSEL structure and provides the key parameters, resonant wavelength, and far-field pattern. A new boundary condition between the emitting surfaces and incident planes is derived based on the scattering matrix method. A doubling scattering matrix method is employed to reduce the total number of calculation steps for a DBR [17].

This paper is organized as follows. Section 2 explains the RCWA algorithm and improved scattering matrix method. In Section 3, the performance of the new algorithm is demonstrated for several structures, including photonic crystal DBR VCSEL and PCSEL designs. This study provides a new method for modelling full VCSELs with periodic structured layers using an efficient RCWA algorithm, which is beneficial for the design and optimization of VCSELs and PCSELs for various applications.

2. RCWA formula

For a periodic structure in the x-y plane, as shown in Fig. 1, only the geometry of a unit cell is necessary to constructed in the RCWA algorithm. The RCWA calculations can be divided into two parts.

1. Calculate the characteristic property of a single layer. This part has been thoroughly demonstrated in literature [17,23–25].

2. Connect multilayer solutions via boundary conditions, including reflection and transmission regions. The new formula applies in this part.

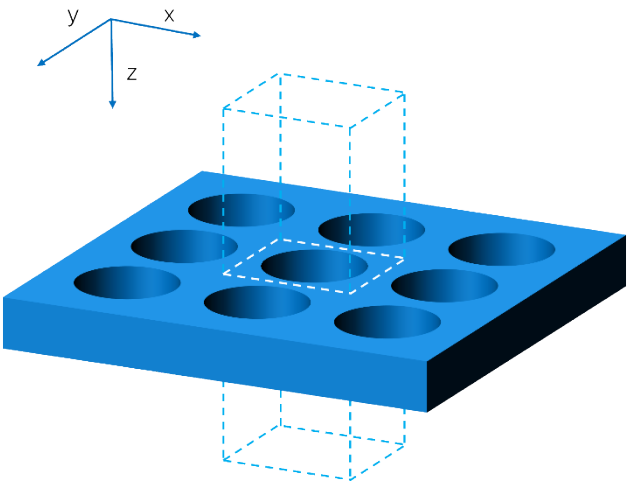

Fig. 1. Schematic of a single layer 2D photonic crystal air hole model.

Optics EXPRESS

2.1. Scattering matrix

The scattering matrix (S matrix) method is implemented in the RCWA algorithm. The S matrix is of the form:

$$\boldsymbol{S} = \begin{bmatrix} \boldsymbol{S}_{11} & \boldsymbol{S}_{12} \\ \boldsymbol{S}_{21} & \boldsymbol{S}_{22} \end{bmatrix} \tag{1}$$

It connects the modes on the outer sides of the boundaries of a layer. The relation between the modes in and out of layer i is described by Eq. 2 and Fig. 2.

$$\begin{bmatrix} \boldsymbol{c}_0^- \\ \boldsymbol{c}_1^+ \end{bmatrix} = \begin{bmatrix} \boldsymbol{S}_{11}^i & \boldsymbol{S}_{12}^i \\ \boldsymbol{S}_{21}^i & \boldsymbol{S}_{22}^i \end{bmatrix} \begin{bmatrix} \boldsymbol{c}_0^+ \\ \boldsymbol{c}_1^- \end{bmatrix} \tag{2}$$

$$\boldsymbol{S}_{11}^i = \boldsymbol{S}_{22}^i = (\boldsymbol{A}_1 - \boldsymbol{X}_i\boldsymbol{B}_i\boldsymbol{A}_i^{-1}\boldsymbol{X}_i\boldsymbol{B}_i)^{-1}(\boldsymbol{X}_i\boldsymbol{B}_i\boldsymbol{A}_i^{-1}\boldsymbol{X}_i\boldsymbol{A}_i - \boldsymbol{B}_i) \tag{3}$$

$$\boldsymbol{S}_{12}^i = \boldsymbol{S}_{21}^i = (\boldsymbol{A}_1 - \boldsymbol{X}_i\boldsymbol{B}_i\boldsymbol{A}_i^{-1}\boldsymbol{X}_i\boldsymbol{B}_i)^{-1}\boldsymbol{X}_i(\boldsymbol{A}_i - \boldsymbol{B}_i\boldsymbol{A}_i^{-1}\boldsymbol{B}_i) \tag{4}$$

where $\boldsymbol{A_i} = \boldsymbol{W_i}^{-1}\boldsymbol{W}_0 + \boldsymbol{V_i}^{-1}\boldsymbol{V}_0, \boldsymbol{B_i} = \boldsymbol{W_i}^{-1}\boldsymbol{W}_0 - \boldsymbol{V_i}^{-1}\boldsymbol{V}_0$ and $\boldsymbol{X_i} = \exp(-\boldsymbol{\lambda}_i k_0 L_i)$. $\boldsymbol{W}$, $\boldsymbol{V}$ and $\boldsymbol{\lambda}$ are notations in [17]. The subscript i indicates the index of layer. $\boldsymbol{c}$ is an arbitrary vector. The superscript indicates the propagating direction . The subscript indicates the position of the vector.

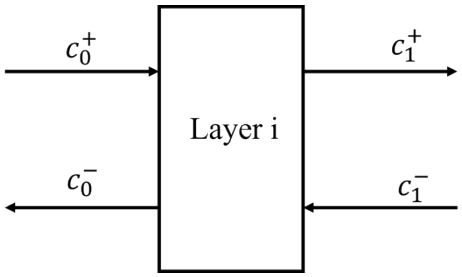

Fig. 2. Demonstration of mode propagation in multilayer structure.

For multilayer structures, a global S matrix is calculated from the S matrix of each layer using the Redheffer star product [17]. This calculation results in a global matrix relating the incident, transmitted, and reflected fields to one another, as shown in Fig. 3. The Redheffer star product $\otimes$ is defined as:

$$\begin{bmatrix} \boldsymbol{C}_{11} & \boldsymbol{C}_{12} \\ \boldsymbol{C}_{21} & \boldsymbol{C}_{22} \end{bmatrix} = \begin{bmatrix} \boldsymbol{A}_{11} & \boldsymbol{A}_{12} \\ \boldsymbol{A}_{21} & \boldsymbol{A}_{22} \end{bmatrix} \otimes \begin{bmatrix} \boldsymbol{B}_{11} & \boldsymbol{B}_{12} \\ \boldsymbol{B}_{21} & \boldsymbol{B}_{22} \end{bmatrix} \tag{5}$$

$$\boldsymbol{C}_{11} = \boldsymbol{A}_{11} + \boldsymbol{A}_{12}[\boldsymbol{I} - \boldsymbol{B}_{11}\boldsymbol{A}_{22}]^{-1}\boldsymbol{B}_{11}\boldsymbol{A}_{21} \tag{6}$$

$$\boldsymbol{C}_{12} = \boldsymbol{A}_{12}[\boldsymbol{I} - \boldsymbol{B}_{11}\boldsymbol{A}_{22}]^{-1}\boldsymbol{B}_{12} \tag{7}$$

$$\boldsymbol{C}_{21} = \boldsymbol{B}_{21}[\boldsymbol{I} - \boldsymbol{A}_{22}\boldsymbol{B}_{11}]^{-1}\boldsymbol{A}_{21} \tag{8}$$

$$\boldsymbol{C}_{22} = \boldsymbol{B}_{22} + \boldsymbol{B}_{21}[\boldsymbol{I} - \boldsymbol{A}_{22}\boldsymbol{B}_{11}]^{-1}\boldsymbol{A}_{22}\boldsymbol{B}_{12} \tag{9}$$

Global scattering matrix S is obtained by continued Redheffer Star product of S matrixes.

$$\boldsymbol{S} = \boldsymbol{S_{ref}} \otimes \boldsymbol{S}_1 \otimes \ldots \otimes \boldsymbol{S_n} \otimes \boldsymbol{S_{trn}} \tag{10}$$

The relation between the incident ($\boldsymbol{e_{inc}}$), transmitted ($\boldsymbol{e_{trn}}$), and reflected ($\boldsymbol{e_{ref}}$) electric fields is described by the global S matrix, which is expressed in Eqs. 11–16. $\boldsymbol{W_{ref}}$ and $\boldsymbol{W_{trn}}$ are identity

Optics EXPRESS

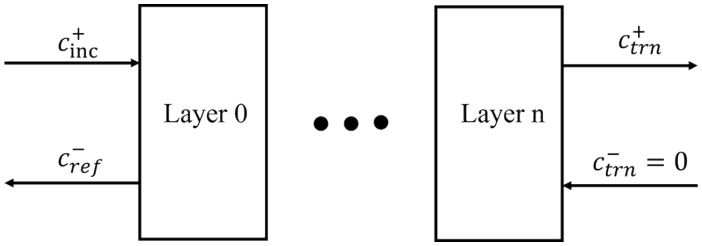

Fig. 3. Demonstration of mode propagation in multilayer structure.

matrixes for homogeneous reflection and transmission regions.

$$\begin{bmatrix} \boldsymbol{c}^-_{\boldsymbol{ref}} \\ \boldsymbol{c}^+_{\boldsymbol{trn}} \end{bmatrix} = [\boldsymbol{S}] \begin{bmatrix} \boldsymbol{c}^+_{\boldsymbol{inc}} \\ 0 \end{bmatrix} \tag{11}$$

$$\boldsymbol{c}^-_{\boldsymbol{ref}} = \boldsymbol{S}_{11}\boldsymbol{c}^+_{\boldsymbol{inc}} \tag{12}$$

$$\boldsymbol{c}^+_{\boldsymbol{trn}} = \boldsymbol{S}_{21}\boldsymbol{c}^+_{\boldsymbol{inc}} \tag{13}$$

$$\boldsymbol{e}_{\boldsymbol{inc}} = \boldsymbol{W}_{\boldsymbol{ref}}\boldsymbol{c}^+_{\boldsymbol{inc}} \tag{14}$$

$$\boldsymbol{e}_{\boldsymbol{ref}} = \boldsymbol{W}_{\boldsymbol{ref}}\boldsymbol{c}^-_{\boldsymbol{ref}} \tag{15}$$

$$\boldsymbol{e}_{\boldsymbol{trn}} = \boldsymbol{W}_{\boldsymbol{trn}}\boldsymbol{c}^+_{\boldsymbol{trn}} \tag{16}$$

2.2. *Doubling algorithm of scattering matrix method*

The study [17] introduced an efficient scattering matrix for modelling longitudinal periodic multilayer structures, particularly the DBR. First, the S-matrix of the repeating unit stack is computed. For example, there are $\boldsymbol{L}$ layers in the repeating unit stack. The S matrix of this repeating stack is represented by Eq. 17. Superscript $\times 1$ indicates only one repeating unit.

$$\boldsymbol{S}^{\times 1} = \boldsymbol{S}^1 \otimes \ldots \otimes \boldsymbol{S}^{\boldsymbol{L}} \tag{17}$$

Then, the S matrix of m units $\boldsymbol{S}^{\times m}$ is given by Eq. 18. Where $m = 2^n, n \in N$.

$$\boldsymbol{S}^{\times \boldsymbol{m}} = \boldsymbol{S}^{\times \frac{\boldsymbol{m}}{2}} \otimes \boldsymbol{S}^{\times \frac{\boldsymbol{m}}{2}} \tag{18}$$

This algorithm transfers the number of units into a binary sequence and performs the Redheffer Star Product of those '1's. For example, a DBR consists of 26 pairs of layers. The binary representation of 26 is 11010. Equation 19 gives the infinite chain of the S matrix where the superscripts are 2^n, n is non-negative integer.

$$\cdots \otimes \boldsymbol{S}^{\times 16} \otimes \boldsymbol{S}^{\times 8} \otimes \boldsymbol{S}^{\times 4} \otimes \boldsymbol{S}^{\times 2} \otimes \boldsymbol{S}^{\times 1} \tag{19}$$

Therefore, only the terms that correspond to '1, $\boldsymbol{S}^{\times 16}, \boldsymbol{S}^{\times 8}$ and $\boldsymbol{S}^{\times 2}$, are stored in memory and computed to obtain $\boldsymbol{S}^{\times 26}$.

$$\boldsymbol{S}^{\times 26} = \boldsymbol{S}^{\times 16} \otimes \boldsymbol{S}^{\times 8} \otimes \boldsymbol{S}^{\times 2} \tag{20}$$

This algorithm reduces the total number of calculation steps. In this example, the doubling algorithm performs only seven Redheffer products. Using the conventional scattering matrix method, the calculation would require 25 products, which is at least three times less efficient than the doubling algorithm.

Optics EXPRESS

2.3. Bidirectional RCWA algorithm

Using RCWA for modelling VCSELs is challenging because the light source is in the middle of the VCSEL structure. As illustrated in Fig. 4, the cavity is located within the VCSEL structure, which is composed of separate multilayer structures on either side. The conventional RCWA algorithm can only simulate with a source from either side of the device. Therefore, researchers typically use FDTD or TMM methods to simulate the output power of a VCSEL. The bidirectional scattering matrix method was developed in a few studies [26,27].

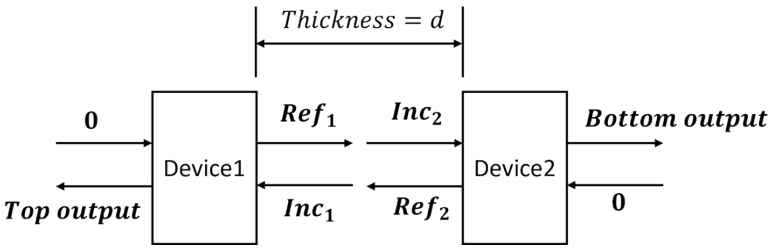

Fig. 4. VCSEL structure illustration.

In Fig. 4, $\boldsymbol{Ref}_1$, $\boldsymbol{Ref}_2$, $\boldsymbol{Inc}_1$, $\boldsymbol{Inc}_2$, ***Top output***, and ***Bottom output*** are vectors of the Fourier coefficients of the electric field propagating in the direction indicated by arrows. Two incident sources are generated at the surfaces of devices 1 and 2, as shown in Fig. 4. Here, the top output power is defined as the output power of the VCSEL.

Our new algorithm utilizes RCWA with the S matrix method to connect the two devices (Device 1 and Device 2 in Fig. 4) and obtain the ratio of the output power to the incident (generated) power from both sides. The S matrix of each device is defined by Eq. 21 where the reflection side is eliminated. A doubling algorithm is employed to expedite the simulation process for the DBR layers.

$$\boldsymbol{S} = \boldsymbol{S}_1 \otimes \ldots \otimes \boldsymbol{S}_n \otimes \boldsymbol{S}_{trn} \tag{21}$$

From Fig. 4, the ***Top output*** and ***Bottom output*** can be derived from the global S matrix formula Eq. 22 and 23, incorporating the incident and reflected fields of both devices. We abbreviate "***Top output***" and "***Bottom output***" as $\boldsymbol{T}$ and $\boldsymbol{B}$ respectively. The region between both the devices is assumed to be a uniform layer.

$$\begin{bmatrix} \boldsymbol{Ref}_1 \\ \boldsymbol{T} \end{bmatrix} = \boldsymbol{S}^1 \begin{bmatrix} \boldsymbol{Inc}_1 + \boldsymbol{X}^{-1}\boldsymbol{Ref}_2 \\ \boldsymbol{0} \end{bmatrix} \tag{22}$$

$$\begin{bmatrix} \boldsymbol{Ref}_2 \\ \boldsymbol{B} \end{bmatrix} = \boldsymbol{S}^2 \begin{bmatrix} \boldsymbol{Inc}_2 + \boldsymbol{X}\boldsymbol{Ref}_1 \\ \boldsymbol{0} \end{bmatrix} \tag{23}$$

$$\boldsymbol{Ref}_1 = \boldsymbol{S}^1_{11}(\boldsymbol{Inc}_1 + \boldsymbol{X}^{-1}\boldsymbol{Ref}_2) \tag{24}$$

$$\boldsymbol{T} = \boldsymbol{S}^1_{21}(\boldsymbol{Inc}_1 + \boldsymbol{X}^{-1}\boldsymbol{Ref}_2) \tag{25}$$

$$\boldsymbol{Ref}_2 = \boldsymbol{S}^2_{11}(\boldsymbol{Inc}_2 + \boldsymbol{X}\boldsymbol{Ref}_1) \tag{26}$$

$$\boldsymbol{B} = \boldsymbol{S}^2_{21}(\boldsymbol{Inc}_2 + \boldsymbol{X}\boldsymbol{Ref}_1) \tag{27}$$

where $\boldsymbol{X} = exp(-\boldsymbol{\lambda}_z k_0 d)$ and $\boldsymbol{X}^{-1} = \exp(\boldsymbol{\lambda}_z k_0 d)$. $\boldsymbol{\lambda}_z = \begin{bmatrix} i\tilde{\boldsymbol{K}}_z & \boldsymbol{0} \\ \boldsymbol{0} & i\tilde{\boldsymbol{K}}_z \end{bmatrix}$ where $\tilde{\boldsymbol{K}}_z = \sqrt{\varepsilon_m \mu_m - \tilde{\boldsymbol{K}}_x^2 - \tilde{\boldsymbol{K}}_y^2}$.

ε_m and μ_m are the relative permittivity and relative permeability of the region between Devices 1 and 2, respectively.

Optics EXPRESS

By substituting 24 into 26 and 26 into 24 separately, the reflection fields of each device can be represented by the known variables.

$$\boldsymbol{Ref}_1 = (\boldsymbol{I} - \boldsymbol{S}_{11}^1 \boldsymbol{X}^{-1} \boldsymbol{S}_{11}^2 \boldsymbol{X})^{-1} (\boldsymbol{S}_{11}^1 \boldsymbol{Inc}_1 + \boldsymbol{S}_{11}^1 \boldsymbol{X}^{-1} \boldsymbol{S}_{11}^2 \boldsymbol{Inc}_2) \tag{28}$$

$$\boldsymbol{Ref}_2 = (\boldsymbol{I} - \boldsymbol{S}_{11}^2 \boldsymbol{X} \boldsymbol{S}_{11}^1 \boldsymbol{X}^{-1})^{-1} (\boldsymbol{S}_{11}^2 \boldsymbol{Inc}_2 + \boldsymbol{S}_{11}^2 \boldsymbol{X} \boldsymbol{S}_{11}^1 \boldsymbol{Inc}_1) \tag{29}$$

where I denotes an identity matrix. Substituting expressions 28 into 27 and 29 into 25 separately yields

$$\boldsymbol{T} = \boldsymbol{S}_{21}^1 \boldsymbol{Inc}_1 + \boldsymbol{S}_{21}^1 \boldsymbol{X}^{-1} (\boldsymbol{I} - \boldsymbol{S}_{11}^2 \boldsymbol{X} \boldsymbol{S}_{11}^1 \boldsymbol{X}^{-1})^{-1} (\boldsymbol{S}_{11}^2 \boldsymbol{Inc}_2 + \boldsymbol{S}_{11}^2 \boldsymbol{X} \boldsymbol{S}_{11}^1 \boldsymbol{Inc}_1) \tag{30}$$

$$\boldsymbol{B} = \boldsymbol{S}_{21}^2 \boldsymbol{Inc}_2 + \boldsymbol{S}_{21}^2 \boldsymbol{X} (\boldsymbol{I} - \boldsymbol{S}_{11}^1 \boldsymbol{X}^{-1} \boldsymbol{S}_{11}^2 \boldsymbol{X})^{-1} (\boldsymbol{S}_{11}^1 \boldsymbol{Inc}_1 + \boldsymbol{S}_{11}^1 \boldsymbol{X}^{-1} \boldsymbol{S}_{11}^2 \boldsymbol{Inc}_2) \tag{31}$$

Subsequently, the electric fields of ***Top output*** and ***Bottom output*** in Fourier space can be computed. The output power can be readily calculated in the same way as the classic RCWA.

2.4. Far-field realization

The far-field pattern can be obtained from the near-field to far-field transformation (Fraunhofer diffraction theory) [28]. The near-field pattern can be reconstructed using the final field Fourier coefficients obtained from RCWA [29,30]. The field in each unit cell is then repeated according to the period of the real device. To obtain a high-resolution far-field pattern, the near field should be sufficiently large according to the Fraunhofer diffraction theory, and the field of the area outside the device should be set to zero.

3. Numerical examples

This algorithm was tested using VCSEL and PCSEL schematics. Lumerical FDTD was also utilized to compare the accuracy and execution time. Mesh quality of 6 (24 points per wavelength) was used in Lumerical FDTD with periodic boundary conditions in the transverse plane. The photonic crystal DBR VCSEL designs in [7] and a PCSEL design example were constructed to verify the accuracy of the new algorithm. The light sources, Inc_1 and Inc_2, as illustrated in Fig. 5, are set to be plane waves propagating perpendicularly towards the top and bottom sides of the device, respectively.

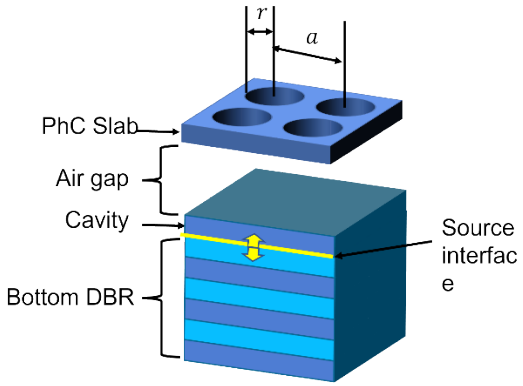

Fig. 5. Schematic of photonic crystal VCSEL design.

The RCWA algorithm and Lumerical FDTD are both executed on an Intel i5-10400F @2.9 GHz CPU using the Intel MKL library.

For the far-field test, the projection pattern of a photonic crystal VCSEL design was computed using the VCSEL RCWA and Rsoft FullWAVE software (FDTD method).

Optics EXPRESS

3.1. Photonic crystal VCSEL

A schematic of the photonic crystal VCSEL is shown in Fig. 5, and Table 1 provides the details of the structure.

Table 1. Material and geometry details of photonic crystal VCSEL structure

Layer	Thickness (nm)	Refractive index n
PhC Slab	230	3.53 and 1.00 (holes)
Air gap	800	1.00
Cavity	60.198	3.53
Bottom DBR × 27	70.132	3.03
	60.198	3.53

Five designs were used in the experiment; the periodicity a was set to 446 nm while varying the radius r to $0.41a$, $0.45a$ and $0.48a$. At radius $r = 0.48$, the periodicity a is then switched to 426 nm and 486 nm.

Figure 6 first demonstrates convergence of the resonant wavelength of the photonic crystal VCSEL designs for several different numbers of harmonics. Harmonics is an important concept defined as the total Fourier order used in an RCWA simulation. Total number of harmonics is calculated as the square of harmonics in one direction. Compared with 25*25 harmonics, 7*7 harmonics shows less than 1E-3 error in the resonant wavelength across the 5 designs. Therefore, in the following experiment, RCWA simulation uses 7 harmonics.

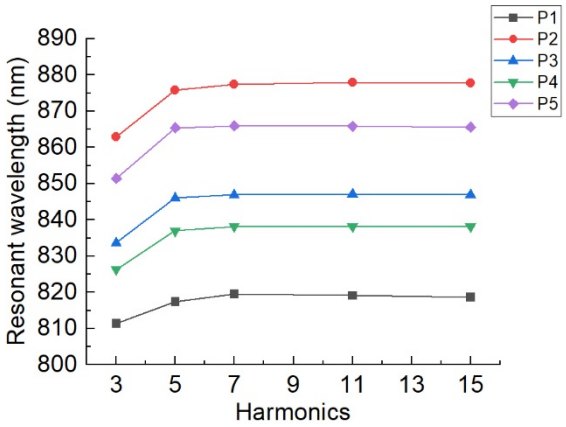

Fig. 6. The resonant wavelength against number of harmonics in one direction used in RCWA.

The execution time and resonant wavelengths of both methods are recorded for wavelengths ranging from 800 nm to 900 nm with increment of 0.1 nm. The RCWA method used seven harmonics, whereas the FDTD method used mesh 6. The calculated resonant wavelengths are compared with a reference FDTD results presented in the literature [7].

Table 2 lists the resonant wavelengths, showing that the difference between RCWA and FDTD reference is less than 3 nm. The Q factor are also calculated and in line with the reference values. The deviation may be caused by the very high number of Q-value where the difference between resonant wavelength and wavelength at half peak are significantly small. The calculated Q factors are very sensitive to the wavelength sweep step and accuracy of RCWA. The power spectrum in Fig. 7 shows distinct peaks. Furthermore, Table 3 indicates that for obtaining accurate results

Optics EXPRESS

(RCWA 7 harmonics and FDTD mesh 6), the RCWA algorithm is about 10-12 times faster than FDTD.

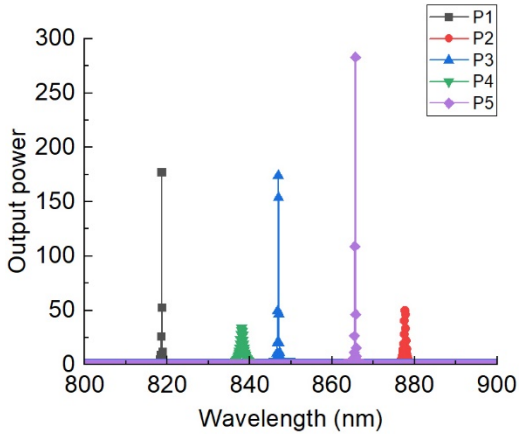

Fig. 7. The resonant wavelength of the planar PhC VCSELs with various designs. The plot number is referred in Table 2.

Table 2. Resonant wavelength and cavity Q factors calculated by RCWA (7 harmonics), Lumerical FDTD (mesh 6) and FDTD from literature [14] are compared for PhC VCSEL designs

Plot	r	a	RCWA (nm)	FDTD Lumerical (nm)	FDTD reference (nm)	RCWA Q factor	Reference Q factor
P1	0.41a	446	819.6	818.0	820.4	9632	12090
P2	0.45a	446	877.4	875.4	877.9	1755	1397
P3	0.48a	446	846.9	847.1	849.8	4210	4354
P4	0.48a	426	838.1	837.5	840.0	839	778
P5	0.48a	486	865.9	864.6	868.9	7868	6225

Table 3. Speed comparison of RCWA and Lumerical FDTD of PhC VCSEL design

Method	$r = 0.41a$ $a = 446nm$	$r = 0.45a$ $a = 446nm$	$r = 0.48a$ $a = 446nm$	$r = 0.48a$ $a = 426nm$	$r = 0.48a$ $a = 486nm$
FDTD mesh 6	1008s	989s	1028s	967s	1050s
RCWA harmonics 7	92.8s	91.8s	86.9s	86.8s	88.3s

3.2. PCSEL

The RCWA algorithm also works accurately for PCSEL structures, such as that in Fig. 8. The details of each layer are presented in Table 4. The photonic crystal layer is a square-lattice air-hole model. The lattice constant is 300 nm. The filling factor (FF) is defined as the area of the air hole over the area of the unit cell. A convergence test was performed for a filling factor of 0.25, as shown in Fig. 9. The mode wavelengths also converge at approximately seven harmonics. Then, resonant wavelengths of FF that equals to 0.1,0.15, 0.2 and 0.25 obtained from RCWA and Lumerical FDTD, are plotted in Fig. 10. The wavelength range for both methods is 950–1050 nm with 0.1 nm step. The results show that the wavelengths obtained from both methods differ by

Optics EXPRESS

a maximum of 2 nm. The average time taken is 71.52s and 2567s for the RCWA program and Lumerical FDTD, respectively. This RCWA program performs 35x faster than the FDTD one. This is because, for band-edge mode PCSEL, FDTD requires a very long time to allow resonance to occur inside the structure.

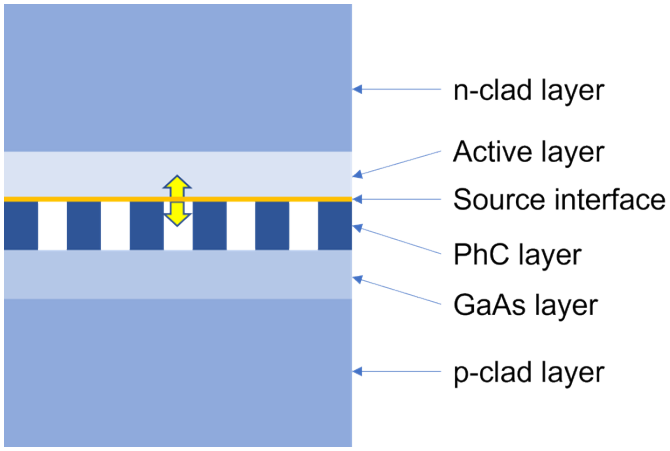

Fig. 8. Schematic cross-sectional of a PCSEL design.

Table 4. Material and geometry details of the example PCSEL structure

Layer	Thickness (μm)	Relative permittivity
n-clad	1.5	11.0224
Active	0.05	13.9876
PhC	0.1	12.7449 and 1 (holes)
GaAs	0.05	12.7449
p-clad	1.5	11.0224

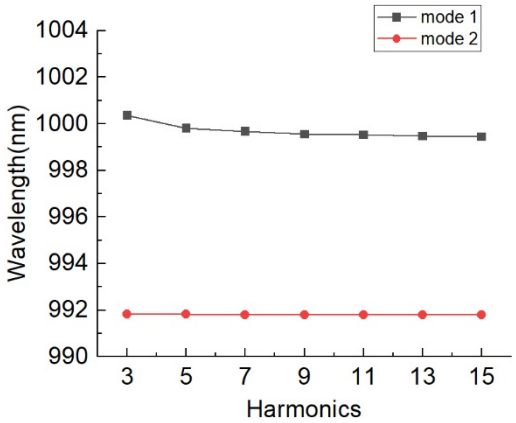

Fig. 9. The resonant wavelength against number of harmonics in one direction used in RCWA.

Optics EXPRESS

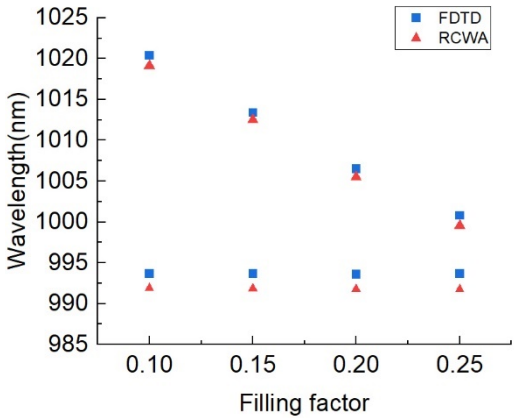

Fig. 10. The first two resonant wavelengths of the PCSEL simulated by FDTD and RCWA.

3.3. *Far-field pattern*

The far-field projection pattern of photonic crystal VCSEL design P5 in Table 2 is generated using the RCWA and Rsoft FullWAVE.

Figures 11–13 show the normalized far field pattern of 5×5,10×10, 15×15 periods of the photonic crystal unit cells, respectively. The full width at half maximum (FWHM) are listed in Table 5.

Table 5. Far field FWHM of the example VCSEL structure using RCWA and Rsoft

Size	RCWA(deg)	Rsoft(deg)
5×5	13.87	14.05
10×10	6.85	7.22
15×15	4.78	5.08

The divergence angle result shows good agreement with Rsoft simulation. The small difference in the graph presentation may be caused by the approximation of finite periods device. The field distortion caused by the edge is not considered in RCWA. For even larger VCSEL or PCSEL design with hundreds of periods of photonic crystal which is impractical to be simulated with FDTD, RCWA method is an efficient way to obtain approximated results.

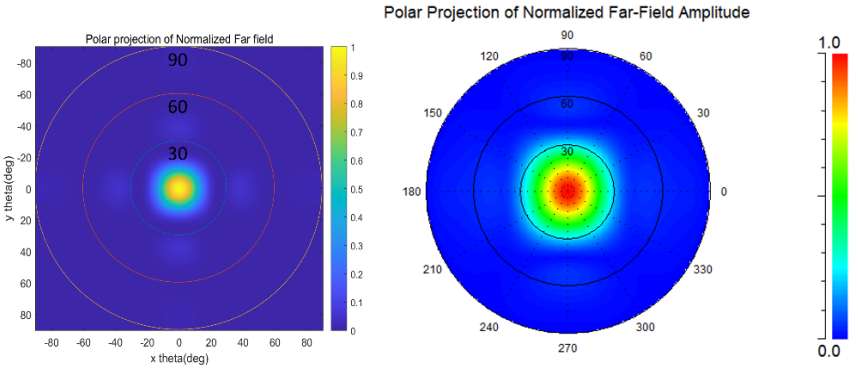

Fig. 11. Far-field of 5×5 periods of photonic crystal cells generated from left. The new RCWA and right. Rsoft FullWAVE.

Optics EXPRESS

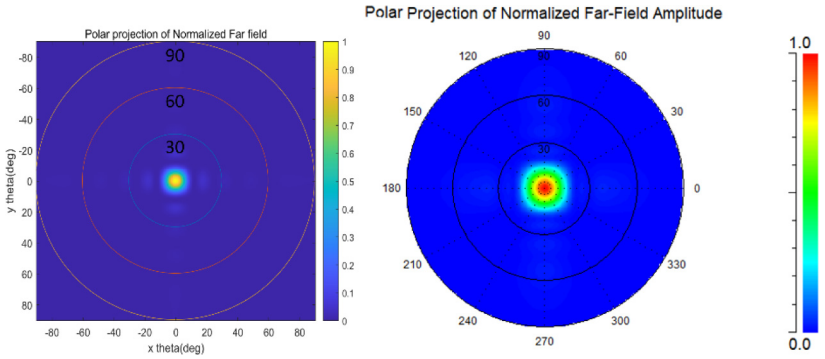

Fig. 12. Far-field of 10×10 periods of photonic crystal cells generated from left. The new RCWA and right. Rsoft FullWAVE.

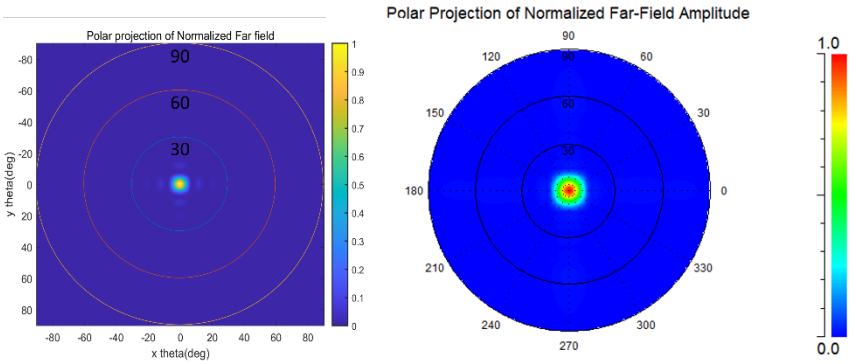

Fig. 13. Far-field of 15×15 periods of photonic crystal cells generated from left. The new RCWA and right. Rsoft FullWAVE.

4. Conclusion

In this work, we presented an integrated RCWA algorithm that efficiently calculates the output power and far field pattern of full VCSEL and PCSEL designs in which a light source is generated from the inside. The results are compared with those of Lumerical FDTD and Rsoft FullWAVE. The RCWA method accurately determines the resonant wavelength with a maximum discrepancy of 3 nm against the reference or Lumerical results. Q factors are calculated to be in line with reference values. The far-field pattern of large finite periodic VCSEL can also be accurately approximated using the RCWA. The results show a difference of less than 0.5° in the divergence angle calculated from the RCWA and Rsoft FDTD. The output quantities of this method are not limited to this article. More quantities can be obtained from postprocessing the simulated electromagnetic fields.

Moreover, the RCWA algorithm demonstrates impressive speedups for different designs. For photonic crystal DBR VCSELs, RCWA shows a 10x speedup compared to high-resolution FDTD. For PCSEL, a 35x speedup is obtained. However, it should be noted that the simulation times of RCWA and FDTD can be influenced by many factors, such as the number of wavelength sweeps, structural properties, optimization levels of each algorithm, and hardware specifications.

Overall, the RCWA algorithm provides an efficient and accurate tool for simulating the full VCSEL and PCSEL structures.

Disclosures. The authors declare no conflicts of interest.

Optics EXPRESS

Data availability. Data underlying the results presented in this paper are not publicly available at this time but may be obtained from the authors upon reasonable request.

References

1. F. Koyama, "Recent Advances of VCSEL Photonics," J. Lightwave Technol. **24**(12), 4502–4513 (2006).
2. T. Hariyama, P. A. M. Sandborn, M. Watanabe, *et al.*, "range-sensing system based on FMCW using low-cost VCSEL," Opt. Express **26**(7), 9285–9297 (2018).
3. S. Ishimura, R. Morita, T. Inoue, *et al.*, "Proposal and Demonstration of Free-Space Optical Communication Using Photonic Crystal Surface-Emitting Lasers," J. Lightwave Technol. **41**(12), 3688–3694 (2023).
4. H. Yu, L. Wang, J. Xu, *et al.*, "A dToF Ranging Sensor with Accurate Photon Detector Measurements for LiDAR Applications," Sensors **23**(6), 3011 (2023).
5. M. D. Zoysa, R. Sakata, K. Ishizaki, *et al.*, "Non-mechanical three-dimensional LiDAR system based on flash and beam-scanning dually modulated photonic crystal lasers," Optica **10**(2), 264–268 (2023).
6. I.-S. Chung, V. Iakovlev, A. Sirbu, *et al.*, "Broadband MEMS-Tunable High-Index-Contrast Subwavelength Grating Long-Wavelength VCSEL," IEEE J. Quantum Electron. **46**(9), 1245–1253 (2010).
7. J. H. Kim, L. Chrostowski, E. Bisaillon, *et al.*, "DBR, Sub-wavelength grating, and Photonic crystal slab Fabry-Perot cavity design using phase analysis by FDTD," Opt. Express **15**(16), 10330–10339 (2007).
8. M. Yoshida, M. D. Zoysa, K. Ishizaki, *et al.*, "Photonic-crystal lasers with high-quality narrow-divergence symmetric beams and their application to LiDAR," J. Phys. Photonics **3**(2), 022006 (2021).
9. K. Hirose, Y. Kurosaka, A. Watanabe, *et al.*, "Realization of high-power narrow beam divergence in photonic-crystal surface-emitting laser," Proc. SPIE **9002**, 90021J (2014).
10. R. Michalzik, *VCSELs* (Springer, 2012), Chap. 2.
11. P. Qiu, W. Pang, P. Fu, *et al.*, "Numerical investigation of vertical-cavity surface-emitting lasers incorporating a high-contrast grating using 3-D FDTD method," Optik **218**, 165125 (2020).
12. W. Liao, C. Li, J. Li, *et al.*, "Polarization control and mode optimization of 850 nm multi-mode VCSELs using surface grating," Appl. Phys. B **127**(2), 23 (2021).
13. M. G. Moharam and T. K. Gaylord, "Rigorous coupled-wave analysis of planar-grating diffraction," J. Opt. Soc. Am. **71**(7), 811–818 (1981).
14. L. Li, "New formulation of the Fourier modal method for crossed surface-relief gratings," J. Opt. Soc. Am. A **14**(10), 2758–2767 (1997).
15. G. L. Whitworth, J. Jaramillo-Fernandez, J. A. Pariente, *et al.*, "Simulations of micro-sphere/shell 2D silica photonic crystals for radiative cooling," Opt. Express **29**(11), 16857–16866 (2021).
16. H. Ding, T. Fan, L. Zhang, *et al.*, "Three-dimensional plasmonic lithography imaging modeling based on the RCWA algorithm for computational lithography," Opt. Express **31**(22), 36061–36077 (2023).
17. R. C. Raymond, "Improved formulation of scattering matrices for semi-analytical methods that is consistent with convention," Prog. Electromagn. Res. B **35**, 241–261 (2011).
18. L. Li, "Formulation and comparison of two recursive matrix algorithms for modeling layered diffraction gratings," J. Opt. Soc. Am. A **13**(5), 1024–1035 (1996).
19. M. G. Moharam, D. A. Pommet, E. B. Grann, *et al.*, "Stable implementation of the rigorous coupled-wave analysis for surface-relief gratings: enhanced transmittance matrix approach," J. Opt. Soc. Am. A **12**(5), 1077–1086 (1995).
20. Y. Liang, C. Peng, K. Sakai, *et al.*, "Three-dimensional coupled-wave model for square-lattice photonic crystal lasers with transverse electric polarization: A general approach," Phys. Rev. B **84**(19), 195119 (2011).
21. Z. Wang, Y. Liang, X. Yin, *et al.*, "Analytical coupled-wave model for photonic crystal surface-emitting quantum cascade lasers," Opt. Express **25**(10), 11997 (2017).
22. A. Y. Song, A. R. K. Kalapala, W. Zhou, *et al.*, "First-principles simulation of photonic crystal surface-emitting lasers using rigorous coupled wave analysis," Appl. Phys. Lett. **113**(4), 041106 (2018).
23. M. G. Moharam, E. B. Grann, D. A. Pommet, *et al.*, "Formulation for stable and efficient implementation of the rigorous coupled-wave analysis of binary grating," J. Opt. Soc. Am. A **12**(5), 1068–1076 (1995).
24. J. Li, L. Shi, D. Ji, *et al.*, "Efficient Implementation of Fourier Modal Method for 2-D Periodic Structures," IEEE Microw. Wireless Compon. Lett. **32**(5), 375–378 (2022).
25. P. Lalanne and G. M. Morris, "Highly improved convergence of the coupled-wave method for TM polarization," J. Opt. Soc. Am. A **13**(4), 779–784 (1996).
26. K. Postava, T. Fördös, H. Jaffrès, *et al.*, "Modeling of anisotropic grating structures with active dipole layers," Proc. SPIE **9516**, 95160O (2015).
27. S. Park, J. Hahn, and H. Kim, "Fourier Modal Method for Optical Dipole Radiation in Photonic Structures," Current Optics and Photonics **5**(6), 597–605 (2021).
28. B. E. A. Saleh and M. C. Teich, *Fundamentals of Photonics* (Wiley, 1991), Chap. 4.
29. P. Lalanne and M. P. Jurek, "Computation of the near-field pattern with the coupled-wave method for transverse magnetic polarization," J. Mod. Opt. **45**(7), 1357–1374 (1998).
30. M. Weismann, D. F. Gallagher, and N. C. Panoiu, "Accurate near-field calculation in the rigorous coupled-wave analysis method," J. Optics **17**(12), 125612 (2015).